Check for updates

Nontoxic Tb³⁺-induced hyaluronic nano-poached egg aggregates for colorimetric and luminescent detection of Fe³⁺ ions†

Jing Wang, [ID] [a] Bei Qian,*[b] Tao Wang, [ID] [a] Yanyan Ma, [ID] [a] Haitao Lin,[a] Yimeng Zhang,[a] Hongmin Lv, [ID] [a] Xiaonan Zhang,[a] Yimeng Hu,[a] Shanshan Xu,[a] Fengchen Liu,[c] Huiling Li[d] and Zike Jiang*[a]

This study demonstrates that a luminescent Tb³⁺ complex with green emission can be complexed with hyaluronic (hya) to form nanoparticles. The structure of complexation is composed of a Tb(acac)₂phen core with a hya surface, similar to those of the nano-poached eggs. What makes the structure unique is that Tb(acac)₂phen and hya are connected by chemical bonds. To confirm their utility, we illustrate that the luminescence is rapidly and selectively quenched in the presence of Fe³⁺. Initial cytotoxicity experiments with human liver carcinoma cells show that the luminescent lanthanide complexes are cytotoxic, however, complexing lanthanides to hya renders them cytocompatible. The new complex integrates the advantages of superior lanthanide luminescence, the unique shape of nano-poached eggs, compatibility with aqueous systems, and cytocompatibility. Tb³⁺-induced hyaluronic nano-poached eggs (THNE) can, therefore, be used for Fe³⁺ detection in aqueous systems.

Introduction

Increasing attention has been focused on environmental and biological detection methods.[1–10] Among them, sensing and imaging technology, as the core of "luminescence", has shown special advantages in environmental monitoring and the diagnosis of diseases.[11–15] The design and discovery of novel sensors for transition-metal ions in aqueous medium are of great concern.[16–20] Fe³⁺ is an essential micronutrient, which plays a critical role in basic physiological processes.[21–23] For example, ferritin is the key to life, which living cells need to survive. Iron ions of ferritin are used to form important intermediates for respiration, photosynthesis, nitrogen fixation, DNA synthesis, *etc.*[24–26] On the other hand, wastewater containing iron discharged from factories, such as acid mining and cleaning rust on steel surfaces, seriously pollutes the environment. Therefore, the detection of Fe³⁺ is an important research field.[27–32]

Lanthanide complexes have bright and narrow emission bands of visible light, fast response times, long fluorescence lifetimes, and very low susceptibility to photobleaching.[33–35] The luminescence of lanthanide ions, such as Tb³⁺ is weak, in part due to its low photon efficiencies. However, lanthanides can be sensitized by complexing them with organic ligands in their first coordination sphere, resulting in the "antenna effect". When complexed to organic ligands, the d–f transitions of Tb³⁺ generate intense luminescence.[36,37] The antenna effect can be used to prepare luminescent complexes with high luminescent efficiency and sharp emission spectra. However, the coordination with organic ligands generally renders lanthanides insoluble in water. Lanthanide–ligand complexation can be dynamic, enabling reversible on–off luminescence. Therefore, changes in the luminescence can be driven by any stimulus that changes the lanthanide–ligand coordination strength, or that introduces competing ligands or competing metal centers leading to cation–ligand exchange. Polymeric materials used as coordinating ligands can provide both dynamic binding and compatibilization with biological and aqueous environments.[38–41]

Biological polysaccharides as ligands of luminescence sensors can modulate the luminescence properties and biological activity.[42] Hyaluronic acid is a polyanion mucopolysaccharide that consists of a basic unit of glucuronic acid and *N*-acetylglucosamine. It is recognized as the best moisturizing ingredient and is widely used in food, medicine and

ᵃInstitute of Oceanographic Instrument, Qilu University of Technology (Shandong Academy of Sciences), Shandong Provincial Key Laboratory of Marine Monitoring Instrument Equipment Technology, National Engineering and Technological Research Center of Marine Monitoring Equipment, 37 Miaoling Road, Qingdao 266061, P. R. China. E-mail: jiangzike2011@126.com

ᵇCollege of Chemistry and Pharmaceutical Sciences, Qingdao Agricultural University, Qingdao 266109, China. E-mail: bqian@qau.edu.cn

ᶜShandong Technological Center of Oceanographic Instrumentation Co., Ltd, 37 Miaoling Road, Qingdao 266061, P. R. China

ᵈInnovation and Development Institute of Shangdong Province, Jinan 250101, P. R. China

cosmetics.[43–45] The integration of natural biomass and luminescence material into one complex can lead to a wide variety of optimized biocompatible materials.[46] Thus, our pioneering experiment has integrated Tb^{3+} superior lanthanide luminescence with the good bio-compatibility of hyaluronic acid. The critical point is that hyaluronic acid modulates both the photophysical properties, morphology and biological activity.

In this work, the original Tb^{3+}-induced hyaluronic nano-poached eggs (THNE) integrates the advantages of superior lanthanide luminescence, the unique shape of nano-poached eggs, compatibility with aqueous systems, and non-toxicity, for the sensing of Fe^{3+} in aqueous surroundings. The lanthanide complexes are cytotoxic but complexing the lanthanides to hyaluronic acid renders them cytocompatible. We reveal the mechanism of luminescence quenching. The luminescence property of THNE is affected by ligand-to-metal charge transfer (LMCT) states. However, the coordination between Fe^{3+} and ligands can alter the LMCT effect of ligands on Tb^{3+}. These properties of THNE have the potential for application in environmental detection systems.

Experimental

Materials

Hyaluronic acid sodium salt from rooster comb (hya) and acetylacetone (acac) were supplied by Shanghai Macklin Biochemical Co. Ltd (Shanghai, China). Terbium chloride hexahydrate ($TbCl_3 \cdot 6H_2O$) was purchased from Sinopharm Chemical Reagent Co. Ltd (Beijing, China). HepG2 was purchased from iCell Bioscience Inc (Shanghai, China). Fetal calf serum was obtained from Biological Industries (Kibbutz Beit-Haemek, Israel). MEM culture medium was purchased from Corning Incorporated (Corning, USA). MTT was supplied by Beijing Solarbio Science & Technology Co. Ltd (Beijing, China). Other chemical reagents were acquired from Shanghai Chemical Reagent Company (Shanghai, China). All water used was deionized. All chemicals mentioned above were of analytical grade.

Preparation of THNEs

THNE was synthesized with magnetic stirring in ethanol–H_2O (3 : 1, v/v). $Tb(acac)_2phen$ was obtained by the complexation of $TbCl_3 \cdot 6H_2O$, acetylacetone (acac) and 1,10-phenanthroline (phen). Here, 1 mL of different concentrations of $TbCl_3 \cdot 6H_2O$ (0.005 M, 0.01 M, 0.02 M, 0.03 M and 0.04 M) and 1 mL of different concentrations of acac (0.01 M, 0.02 M, 0.04 M, 0.06 M and 0.08 M) were mixed and stirred for 30 min at room temperature. Afterwards, the mixture was adjusted to pH 7–8 by using 0.25 M NaOH solution. Then, 1 mL of different concentrations of phen (0.005 M, 0.01 M, 0.02 M, 0.03 M and 0.04 M) was added to the solution and stirred for 2 h. The obtained Tb complexes were colorless and dissolved in ethanol. Next, 1 mL 0.5 mg mL^{-1} hya was added to the Tb complexes and stirred for 2 h (Table 1). We also prepared $Tb(acac)_2phen$ (5.0 mM, Tb^{3+}). $Tb(acac)_2phen$ and THNE with different concentrations were

Table 1 Preparation of THNEs with different concentrations of Tb^{3+}, acac and phen (add 1 mL for each sample)

THNEs	Tb^{3+}	Acac	Phen	Hya
1.25 mM Tb^{3+}	0.005 M	0.01 M	0.005 M	0.5 mg mL^{-1}
2.5 mM Tb^{3+}	0.01 M	0.02 M	0.01 M	0.5 mg mL^{-1}
5.0 mM Tb^{3+}	0.02 M	0.04 M	0.02 M	0.5 mg mL^{-1}
7.5 mM Tb^{3+}	0.03 M	0.06 M	0.03 M	0.5 mg mL^{-1}
10.0 mM Tb^{3+}	0.04 M	0.08 M	0.04 M	0.5 mg mL^{-1}

obtained. The schematic diagram of the synthesis of THNE is shown in Fig. 1.

Luminescence titration experiments

Here, 0.1 M metal chloride salt solutions (Ca^{2+}, Mg^{2+}, K^+, Na^+, Zn^{2+}, Al^{3+}, Mn^{2+}, Cr^{3+}, Ni^{2+}, Cu^{2+}, Co^{2+} and Fe^{3+}) were prepared in water. THNE solution (5.0 mM, Tb^{3+}) was prepared in ethanol–H_2O (3 : 1, v/v). For all measurements of luminescence spectra, the excitation wavelength was 347 nm and the emission slit widths were 5.0 nm. Luminescence titration experiments were performed using THNE solution (5.0 mM, Tb^{3+}) with varying volumes of metal chloride salts. The concentrations of THNE and metal chloride salts were calculated from the luminescence titration experiments.

Cell cytotoxicity experiment

Human liver carcinoma cells HepG2 were incubated on a 96-well plate for 24 h. Culture medium, blank solvent ethanol–H_2O (3 : 1, v/v), hya, $Tb(acac)_2phen$ (5.0 mM, Tb^{3+}), and different concentrations (1.25 mM, 2.5 mM, 5.0 mM, 7.5 mM and 10.0 mM) of the THNE were added to different wells, then the cells were cultured for 24 h. Each condition was prepared in triplicate. HepG2 cells were washed and incubated for 4 h with 100 μL MTT solution. The liquid medium was removed, then 150 μL of DMSO was added to each well, and the crystals in each well were reacted with the DMSO for 1 h. The absorbance measurements of each well were obtained at 570 nm by a multimode plate reader.

Characterization

Photoluminescence spectra were obtained using a fluorescence spectrophotometer (Hitachi Ltd., F-4500, Japan). The excitation and emission wavelengths were fixed at 347 nm and 547 nm. Fluorescence lifetimes and quantum yields were evaluated by a photoluminescence spectrometer (Edinburgh Instruments, FLS1000, UK). The IR spectra $TbCl_3 \cdot 6H_2O$, acac, phen·H_2O, hya, $Tb(acac)_2phen$, and THNE were evaluated by FTIR spectroscopy (Thermo Electron Scientific Instruments Corp., Nicolet iS5, USA). X-ray photoelectron spectra (XPS) of $Tb(acac)_2phen$, hya and THNE were obtained using a spectrometer (Thermo Fisher Scientific Inc., ESCALAB Xi+, USA). The morphology of THNE was characterized by transmission electron microscopy (TEM) (Hitachi Ltd., HT7700, Japan). The size of THNE was determined using a Malvern laser particle size analyzer (Malvern Instruments Ltd., Zetasizer Nano ZSP, UK). Photographs of
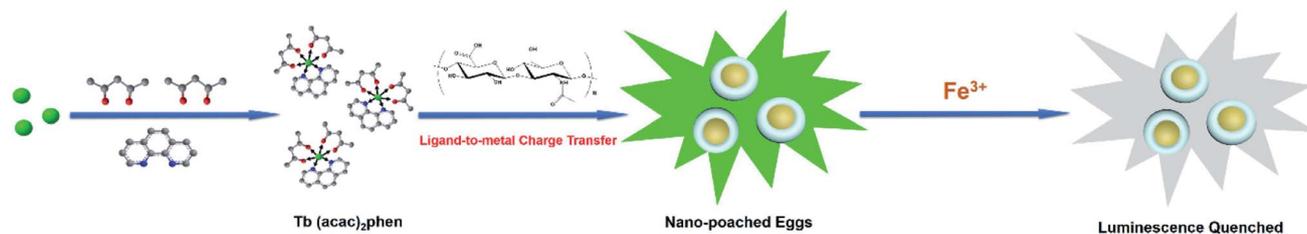
Fig. 1 Schematic diagram of the synthesis of THNE and the quenched effect by Fe^{3+}.

THNE were obtained on illumination by a 365 nm UV lamp (SupFire Photoelectric Equipment Co. Ltd., UV03, China). Cytotoxicity experiments were conducted using a Multimode Reader (Tecan Group Ltd., SPARK 10M, Switzerland). Origin 7.0 software was used to present the experimental results of luminescence spectra, fluorescence lifetimes, FTIR analysis, DLS, XPS, MTT and luminescence response.

Results and discussion

We prepared THNEs with different concentrations (Table 1) in order to screen materials with excellent luminescence properties. Fig. 2a shows luminescence excitation spectra and emission spectra of THNE with different concentrations. A broad band from 310 to 380 nm with the maximum excitation wavelengths of 332 nm, 337 nm, 347 nm, 349 nm and 350 nm was observed in the excitation spectrum of THNE and could be caused by the intraligand $\pi \rightarrow \pi*$ transitions from acac, phen and hya. With the increased concentration of THNE, the maximum excitation wavelength was enhanced. The luminescence emission spectra were obtained by selecting the corresponding maximum excitation wavelength. The characteristic luminescence spectra of Tb^{3+} were obtained with different concentrations of THNE (λ_{em} = 547 nm). With the increase in the concentrations of THNE (less than 5.0 mM Tb^{3+}), the fluorescence intensity was gradually enhanced. However, when the concentrations were more than 5.0 mM Tb^{3+}, the luminescence intensity presented the opposite tendency. When the concentration was 5.0 mM Tb^{3+}, the luminescence intensity was the highest. If the concentration of Tb^{3+} was higher than 5.0 mM, the emission intensity of THNE was decreased. This is called concentration quenching, which is mainly due to a cross-relaxation (CR) process between Tb^{3+}. This phenomenon widely occurs in Tb^{3+}-induced luminescent materials, setting
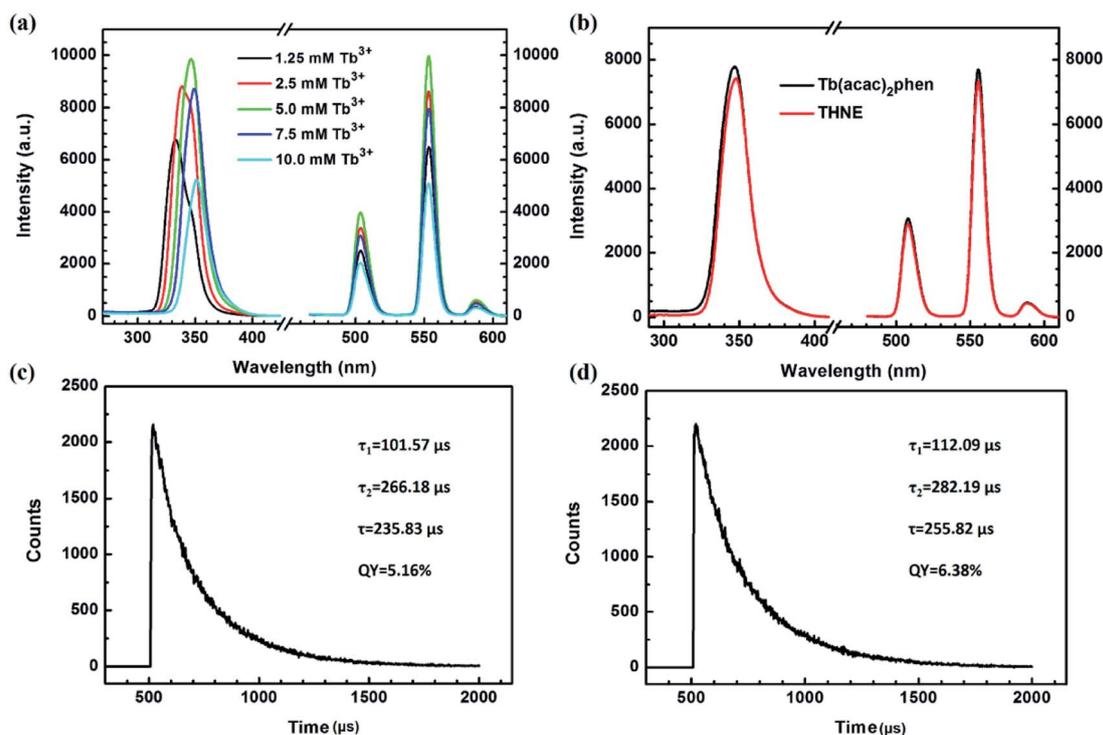

Fig. 2 (a) Luminescence excitation spectra and emission spectra of THNE with different concentrations (λ_{em} = 547 nm, Table 1); (b) luminescence excitation spectra and emission spectra of Tb(acac)$_2$phen and THNE (λ_{ex} = 347 nm, λ_{em} = 547 nm); (c) fluorescence lifetime measurement of THNE; (d) fluorescence lifetime measurement of Tb(acac)$_2$phen.

a limit in the concentration of Tb^{3+} to control the brightness.[47] Therefore, we selected THNE (5.0 mM Tb^{3+}) as an excellent luminescent material.

Fig. 2b displays the luminescence excitation spectra of $Tb(acac)_2phen$ and THNE ($\lambda_{em} = 547$ nm) and the luminescence emission spectra of $Tb(acac)_2phen$ and THNE ($\lambda_{ex} = 347$ nm). THNE also contains the same characteristic emission bands. The luminescence emission spectra of $Tb(acac)_2phen$ and THNE do not have significant differences in their respective emission wavelengths. These represent the band splitting character and $^5D_4-^7F_5$ transition intensities, with those of known complex compounds of Tb^{3+} and the results of f–f transitions of the lanthanide ion. This means that added hya keeps the luminescence properties of the Tb complex. Compared to the luminescence intensity of $Tb(acac)_2phen$, the luminescence intensity of THNE was slightly weakened. We explain why the luminescence intensity of THNE decreased in the further experimental results of XPS analysis (Fig. 3) and morphology (Fig. 4a and b). The fluorescence lifetime of THNE is approximately 235.83 µs and the quantum yield is 5.16% (Fig. 2c). The fluorescence lifetime of $Tb(acac)_2phen$ is approximately 255.82 µs and the quantum yield is 6.38% (Fig. 2d). We also discuss the reasons after the experimental results of XPS and TEM analysis.

Fig. S1† presents the FTIR spectra of $TbCl_3$, acac, phen, hya, $Tb(acac)_2phen$ and THNE. As shown in the FTIR spectrum of acac, the peaks at 1732 and 1709 cm^{-1} characterize the absorptions of the C=O stretching vibration. The significant peaks at 1304, and 1248 cm^{-1} are due to stretching vibration from C–C. The peak at 1420 cm^{-1} is assigned to $-CH_2$ bending vibration, and the $-CH_3$ bending vibration peak is observed at 1360 cm^{-1}. The peak at 1646 cm^{-1} of phen is assigned to the C=N stretching vibration, and the C–N stretching vibration peaks are observed at 1140 and 1090 cm^{-1}. The significant peaks at 1616, 1590, 1506 and 1423 cm^{-1} are due to the stretching vibration of the skeleton from C=C and C=N (pyridine rings). As shown in Fig. S1†† of hya, the absorption at 3421 cm^{-1} was due to the O–H stretching vibration. The trough at 1646 cm^{-1} features the absorption of the C=O stretching vibration. The significant peak at 1400 cm^{-1} is due to the bending vibration absorption from the O–H group. The peak at 1109 cm^{-1} is assigned to the C–O–C stretching vibration of ethers.[48] Compared with the FTIR spectra of hya, $Tb(acac)_2phen$ and THNE, the peaks at 1646 cm^{-1} of the C=O stretching vibration, 1519 cm^{-1} of the pyridine ring stretching vibration, and 1400 cm^{-1} of O–H stretching vibration can be found in THNE. The above data indicate that THNE was prepared successfully.

To further confirm the interaction between the Tb complex and hya, XPS spectra were obtained as shown in Fig. 3. $Tb(acac)_2phen$, hya and THNE were investigated by XPS. The obtained information about typical O 1s peaks are detailed in Fig. 3b, d and f. Fig. 3a shows a typical peak at 530.84 eV in the XPS spectrum of $Tb(acac)_2phen$ representing the O 1s. The peak at 398.87 eV is related to the N 1s of $Tb(acac)_2phen$. The high-resolution spectrum of O 1s (Fig. 3b) shows the peaks at 531.02 and 530.45 eV, which represent C–O and Tb–O.

Comparing the peaks of the samples in Fig. 3b and d, the binding energy of Tb–O was changed and C–O was formed, illustrating that the oxygen atom of $Tb(acac)_2phen$ interacted with hya.[49] Thus, $Tb(acac)_2phen$ and hya created chemical bonds to form THNE. The typical peak at 399.40 eV of hya represents the N 1s (Fig. 3c). The N 1s peak of THNE is 398.97 eV (Fig. 3e). XPS further proves the explanation of the luminescence change after adding hya in Fig. 2b.

The morphology of THNE was investigated via TEM images (Fig. 4a and b) and DLS (Fig. 4d). THNE was dropped onto copper mesh covered with carbon film (230 mesh) and dried by infrared lamp prior to imaging by TEM. The core–shell morphological structure with cavities is shown in Fig. 4a and b. The width of the shell is about 185 nm. The structures of THNE are composed of $Tb(acac)_2phen$ cores with the hya surface. Interestingly, this morphology is very similar to the nano-poached eggs (Fig. 4c). The boiled egg white (hya) wraps its egg yolk ($Tb(acac)_2phen$). What makes the nano-poached egg unique is that the egg white and egg yolk are connected by chemical bonds Tb–O. The size of THNE is distributed in the range of 450 nm to 1000 nm. The circular particles of THNE with a diameter of approximate 700 nm and a broad size distribution are shown in Fig. 4d. A similar structure was reported by Prof. Tang.[46] The nano-dumbbell aggregates were synthesized by combining Eu complexes with hyaluronic acid, which could effectively load drugs and sense drugs.

Hya has good water solubility and film formation. These core–shell nanoparticles were formed during the coordination of $Tb(acac)_2phen$ and hya when the samples were stirred at high speed in the ethanol–H_2O (3 : 1, v/v) system. A constant magnetic stirring of 1500 rpm was maintained for 2 h. The complexation of $Tb(acac)_2phen$ and hya was proved by XPS (Fig. 3). However, as we know, when Tb^{3+} interacts with sensitizing ligands the "antenna effect" occurs. These ligands sensitize the luminescence of rare earth ions and enhance the luminescence intensity. This type of luminescence response can be driven by any stimuli that change the lanthanide–ligand coordination strength. Thus, the luminescence intensity of THNE should be greater than that of $Tb(acac)_2phen$. Luminescence data show that the luminescence intensity of THNE is slightly weakened as compared to the luminescence intensity of $Tb(acac)_2phen$ (Fig. 2b). The luminescence intensity of lanthanide complexes is influenced not only by lanthanide–ligand coordination but also the morphology. The Tb^{3+} complex is wrapped by hya, which is similar to putting a non-luminous coat on the green phosphor. Although the coordination between $Tb(acac)_2phen$ and hya enhances the luminescence, the outer film weakens the luminescence; therefore, the synergistic reaction of two factors leads to the decrease in luminescence intensity. Furthermore, on comparing the same type of luminescent materials, the luminescence intensity of THNE is slightly weaker than that of $Tb(acac)_2phen$, and the fluorescence lifetime of THNE (235.83 µs) is shorter than that of $Tb(acac)_2$-phen (255.82 µs).

In order to investigate the detection of metal ions by THNE, the luminescence response with different metal ions was determined. The effects of the metal ions Ca^{2+}, Mg^{2+}, K^+, Na^+,
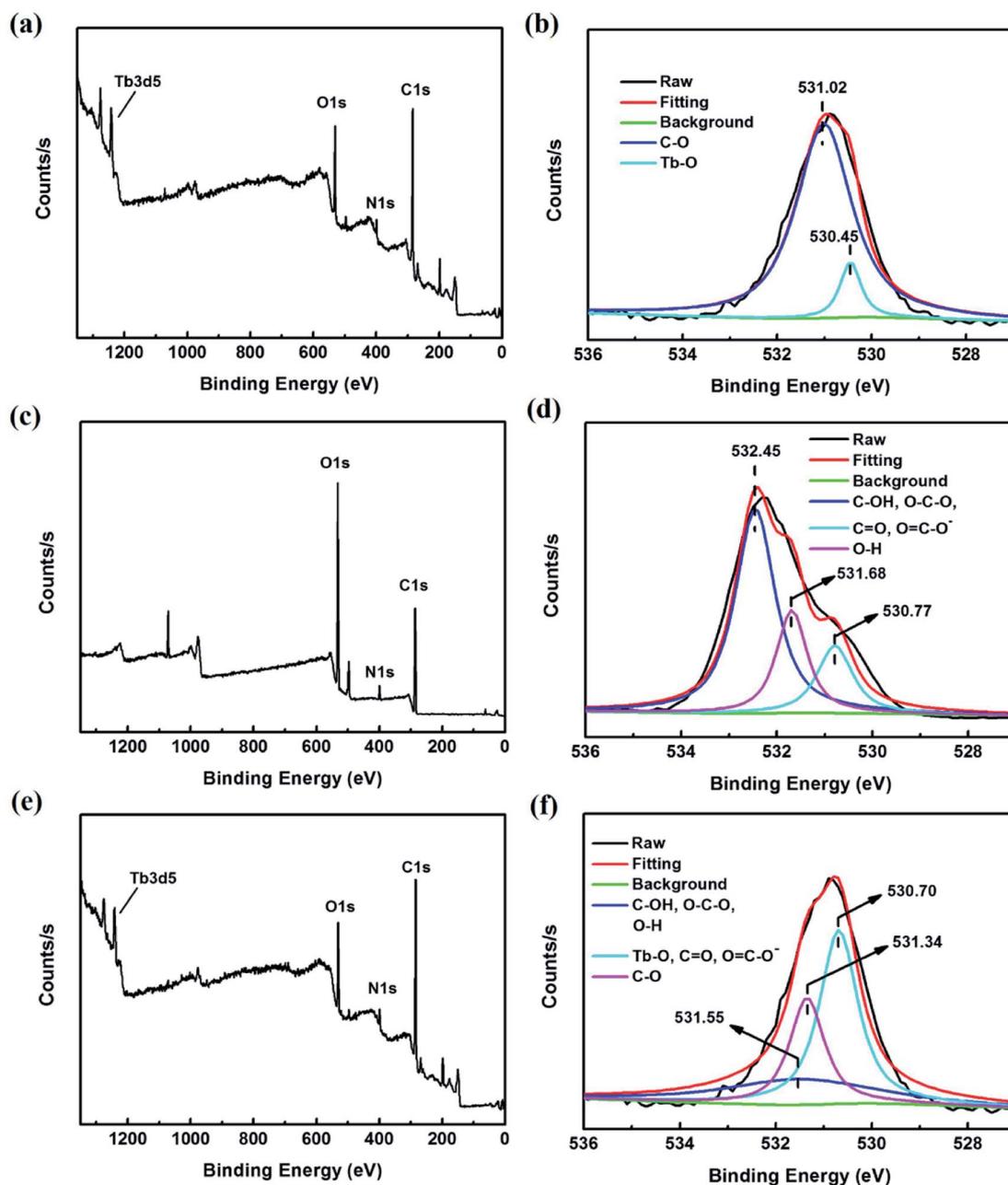
Fig. 3 (a) XPS of Tb(acac)$_2$phen; (b) high-resolution O 1s peak of Tb(acac)$_2$phen; (c) XPS of hya; (d) high-resolution O 1s peak of hya; (e) XPS of THNE; (f) high-resolution O 1s peak of THNE.

Zn^{2+}, Al^{3+}, Mn^{2+}, Cr^{3+}, Ni^{2+}, Cu^{2+}, Co^{2+} and Fe^{3+} in aqueous solution on the luminescence emission of THNE were investigated. Fig. 5d shows the luminescence response of THNE with the addition of 10 μL (250 μM in THNE) of various metal ions. I_0 and I are the luminescence intensities of THNE in0 μL (0 μM) and 10 μL (250 μM in THNE) of different metal ions. THNE is much more sensitive to Fe^{3+} than to the other cations. When Fe^{3+} (250 μM) was added to the THNE, the luminescence intensity at 547 nm was reduced by more than 90%. When 10 μL Ca^{2+}, Mg^{2+}, K^+, and Na^+ were added, the luminescence intensity remained the same. The THNE retained more than 80% of the

luminescence in 10 μL Zn^{2+}, Al^{3+}, and Mn^{2+}. When 10 μL Cr^{3+}, Ni^{2+}, Cu^{2+}, and Co^{2+}, were added, more than 40% of the luminescence intensity was retained. Among these various metal ions, THNE shows a selective luminescence response to Fe^{3+} in aqueous solution. In order to visually describe the changes in the luminescence intensity when different metal ions were added, we present photos of naked-eye-visible and 365 nm UV lamp illumination color changes of THNE (5.0 mM Tb^{3+}) upon the addition of various metal ions (250 μM) in Fig. S2.† After adding Fe^{3+}, the color of THNE changed from colorless to brown, and the green luminescence was quenched under
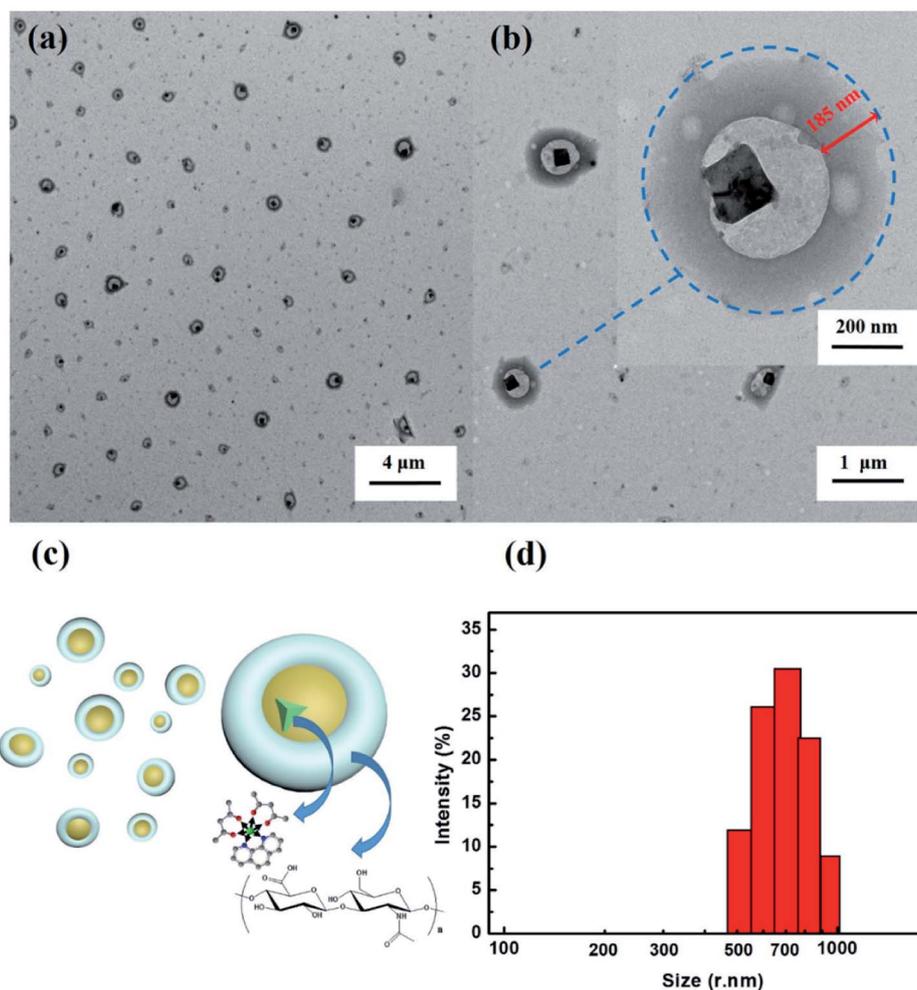
Fig. 4 (a and b) TEM images of THNE; (c) possible nano-poached egg-morphology of THNE; (d) size distribution of THNE by DLS.

a 365 nm UV lamp. However, on adding the other metal ions, we still observed obvious green luminescence.

To further illustrate the luminescence sensing property of THNE, a luminescence titration of THNE was executed by adding different concentrations of Fe^{3+}. Luminescence spectra of THNE in the presence of different concentrations of Fe^{3+} (0–300 μM) are shown in Fig. 5a. The luminescence spectra were obtained by excitation at 347 nm. The representative peak at 547 nm is shown in the luminescence spectrum of THNE. The primary emission peaks show a clear quenching behavior as Fe^{3+} is added. With the concentration of Fe^{3+} increasing, the luminescence intensity gradually decreased until quenched. When 300 μM of Fe^{3+} was added to the THNE, the fluorescence intensity at 547 nm was reduced by more than 90%. In Fig. 5a, the inset shows the ratio of the intensity (I) to the initial intensity (I_0), after the addition of Fe^{3+}. By fitting the experimental data, an excellent curve relationship between I/I_0 and the concentration of Fe^{3+} was obtained over the range from 0 μM to 300 μM. The curve equation is as follows:

$$y = e^{a+bx+cx^2}$$

where $a = -0.054$, $b = -0.011$, and $c = 7.48 \times 10^{-6}$. These results demonstrate that THNE can be used as a sensor for Fe^{3+} in aqueous systems based on a luminescence quenching response. The limit of detection (LOD) of Fe^{3+} sensing was calculated using the following formula:

$$LOD = 3\sigma/S$$

S is the linear slope and σ is the standard deviation of the intensity value of 10 blank samples. By linear fitting at low concentrations of Fe^{3+} (Fig. 5b), the results showed that the LOD is 1.66 μM. In order to visually observe different concentrations of Fe^{3+} added into THNE, we took photos as shown in Fig. 5c. The pictures illustrates that the THNE sample is colorless to the naked eye and exhibits bright green luminescence under the 365 nm UV lamp illumination. After adding different concentrations (A-0 μM, B-25 μM, C-50 μM, D-75 μM, E-100 μM, F-150 μM, G-200 μM, H-250 μM and I-300 μM) of Fe^{3+}, the luminescence intensity decreased gradually until quenched.

The luminescence properties of THNE are affected by ligand-to-metal charge transfer (LMCT) states.[50] The O atom of hya was
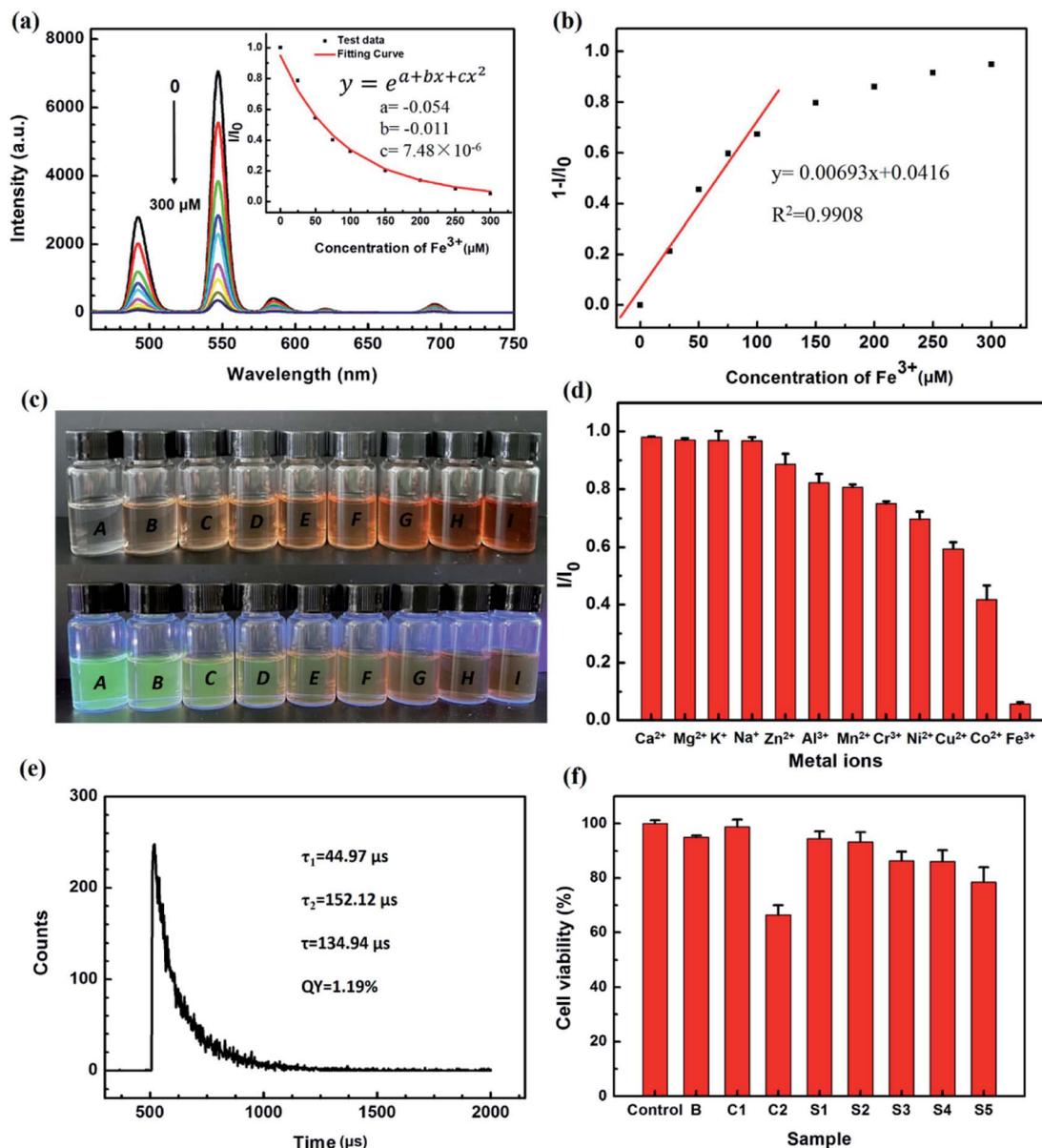
Fig. 5 (a) Luminescence emission spectra of THNE in the presence of different concentrations of Fe^{3+}; inset: the plot of I/I_0 versus the concentration of Fe^{3+}, where I_0 and I are the luminescence intensities of THNE in 0 μM and the various concentrations of Fe^{3+}. (b) The plot of $1 - I/I_0$ versus the concentration of Fe^{3+}. (c) Photographs of THNE with different concentrations of Fe^{3+} (A-0 μM, B-25 μM, C-50 μM, D-75 μM, E-100 μM, F-150 μM, G-200 μM, H-250 μM and I-300 μM) under the naked eye and with 365 nm UV lamp illumination. (d) Luminescence response of THNE to various metal ions with 250 μM; I_0 and I are the luminescence intensities of THNE in 0 μM and 250 μM of Ca^{2+}, Mg^{2+}, K^+, Na^+, Zn^{2+}, Al^{3+}, Mn^{2+}, Cr^{3+}, Ni^{2+}, Cu^{2+}, Co^{2+} and Fe^{3+}, respectively (λ_{ex} = 347 nm, λ_{em} = 547 nm). (e) Fluorescence lifetime measurement of THNE with Fe^{3+}. (f) Cell viability after incubation with culture medium (control), blank solvent ethanol–H_2O (3 : 1, v/v) (B), control sample 1 hya (C1), control sample 2 Tb(acac)$_2$phen (5.0 mM, Tb^{3+}) (C2), and different concentrations (S1-1.25 mM, S2-2.5 mM, S3-5.0 mM, S4-7.5 mM and S5-10.0 mM) of the THNE for 24 h.

coordinated with Tb^{3+} to form the Tb–O chemical bond, leading to the formation of the nano-poached egg structures (Fig. 3f and 4a). With the addition of different metal ions (Ca^{2+}, Mg^{2+}, K^+, Na^+, Zn^{2+}, Al^{3+}, Mn^{2+}, Cr^{3+}, Ni^{2+}, Cu^{2+}, Co^{2+} and Fe^{3+}), Tb^{3+}, metal ions and ligands (acac, phen and hya) formed the balance of the coordination. The results of luminescence titration experiments (Fig. 5d and S2†) can be divided into three types. First, with the metal ions Ca^{2+}, Mg^{2+}, K^+, and Na^+, there were no

luminescence responses. Compared with Tb^{3+}, these metal ions have weak coordination ability with the N and O of ligands. They cannot affect the coordination of THNE. Second, with the metal ions Zn^{2+}, Al^{3+}, Mn^{2+}, Cr^{3+}, Ni^{2+}, Cu^{2+} and Co^{2+}, the luminescence intensity was reduced. This is due to the stronger coordination ability of these metal ions than Tb^{3+} with ligands. Third, the 300 μM concentration of Fe^{3+} quenched the luminescence of THNE. The luminescence intensity gradually

decreased until quenching occurred by the gradual replacement of Tb^{3+} by Fe^{3+}.[27,38] Based on the model of the Tb^{3+}–ligands luminescent material, the Fe^{3+} sensor mechanism can be summarized as follows: the coordination between Fe^{3+} and ligands can alter the LMCT effect of ligands towards Tb^{3+}. The stronger affinity of the ligands' N and O toward Fe^{3+} reduces the efficiency of charge and energy transfer from ligands to Tb^{3+}. This leads to a gradual decrease in the luminescence intensity until quenching occurs. To prove the complexation behavior of THNE with Fe^{3+}, the fluorescence lifetime of THNE with Fe^{3+} (300 μM) is measured in Fig. 5e. The fluorescence lifetime of THNE with Fe^{3+} is 134.94 μs and the quantum yield is 1.19%. The fluorescence lifetime of THNE with Fe^{3+} is greatly weakened as compared to the value of THNE (235.83 μs) as shown in Fig. 2c. The values of τ_1' (44.97 μs) and τ_2' (152.12 μs) are both dramatically reduced as compared with τ_1 (101.57 μs) and τ_2 (266.18 μs) of THNE. These data indicate that on adding Fe^{3+} to THNE, two other Tb^{3+} complexes were obtained.

To prove the non-toxicity of THNE, the cell cytotoxicity experiments were conducted using human liver carcinoma cells, HepG2. Fig. 5f illustrates the culture medium (control), blank solvent ethanol–H_2O (3 : 1, v/v) (B), 0.125 mg mL^{-1} hya (C1), 5.0 mM $Tb(acac)_2$phen (C2) and different concentrations (S1-1.25 mM, S2-2.5 mM, S3-5.0 mM, S4-7.5 mM and S5-10.0 mM) of THNE on HepG2 cells incubated for 24 h. Toxicity is defined here as a 20% reduction in the metabolic activity measured by the MTT assay. From the figure given above, it can be seen that hya almost demonstrated nontoxicity on incubation with HepG2 cells. The sample of 5.0 mM $Tb(acac)_2$phen is cytotoxic to HepG2 cells, exhibiting about a 35% reduction in cell viability. Furthermore, with the integration of the natural polysaccharide hya, the cell viability was significantly improved. The cell viability was more than 80% after incubation with different concentrations of THNE for 24 h, even at much higher concentrations. These results suggest that THNE is non-toxic to cells.

Conclusion

The original Tb^{3+}-induced hyaluronic nano-poached eggs, which integrate the advantages of superior lanthanide luminescence, the unique shape of nano-poached eggs, compatibility with aqueous systems, and non-toxicity, were targeted toward the sensing of Fe^{3+} in aqueous surroundings. The generation of the lanthanide-induced polysaccharide complexes is simple and environmentally friendly. The luminescence intensity of lanthanide complexes is influenced not only by lanthanide–ligand coordination but also by the nanosized morphology. The advantageous properties of the luminescence sensors include high selectivity for Fe^{3+} as compared to other cations, a fast response, bright and narrow luminescence emission bands, and suitability for use in aqueous systems. Future research will optimize lanthanide and polysaccharide-based nanoparticles for the detection of metal ions in aqueous and biological samples.

Conflicts of interest

The authors declare that they have no conflict of interest.

Acknowledgements

References

1 R. George Kerry, K. E. Ukhurebor, S. Kumari, G. K. Maurya, S. Patra, B. Panigrahi, S. Majhi, J. R. Rout, M. d. P. Rodriguez-Torres, G. Das, H.-S. Shin and J. K. Patra, A comprehensive review on the applications of nano-biosensor-based approaches for non-communicable and communicable disease detection, *Biomater. Sci.*, 2021, **9**(10), 3576–3602.

2 H. Huang, W. Feng and Y. Chen, Two-dimensional biomaterials: material science, biological effect and biomedical engineering applications, *Chem. Soc. Rev.*, 2021, **50**(20), 11381–11485.

3 X. Li, H. Wang, Y. Xu, W. Liu, Q. Gong, W. Wang, X. Qiu, J. Zhu, F. Mao, H. Zhang and J. Li, Novel Vilazodone–Tacrine Hybrids as Potential Multitarget-Directed Ligands for the Treatment of Alzheimer's Disease Accompanied with Depression: Design, Synthesis, and Biological Evaluation, *ACS Chem. Neurosci.*, 2017, **8**(12), 2708–2721.

4 M. K. Masud, J. Na, M. Younus, M. S. A. Hossain, Y. Bando, M. J. A. Shiddiky and Y. Yamauchi, Superparamagnetic nanoarchitectures for disease-specific biomarker detection, *Chem. Soc. Rev.*, 2019, **48**(24), 5717–5751.

5 T. M. Reineke, Stimuli-Responsive Polymers for Biological Detection and Delivery, *ACS Macro Lett.*, 2016, **5**(1), 14–18.

6 M. Pirzada and Z. Altintas, Nanomaterials for virus sensing and tracking, *Chem. Soc. Rev.*, 2022, **51**(14), 5805–5841.

7 Y. Shu, Q. Ye, T. Dai, Q. Xu and X. Hu, Encapsulation of Luminescent Guests to Construct Luminescent Metal–Organic Frameworks for Chemical Sensing, *ACS Sens.*, 2021, **6**(3), 641–658.

8 X. Li, F. Jiang, M. Liu, Y. Qu, Z. Lan, X. Dai, C. Huang, X. Yue, S. Zhao, X. Pan and C. Zhang, Synthesis, Characterization, and Bioactivities of Polysaccharide Metal Complexes: A Review, *J. Agric. Food Chem.*, 2022, **70**(23), 6922–6942.

9 S. Chatterjee, X.-Y. Lou, F. Liang and Y.-W. Yang, Surface-functionalized gold and silver nanoparticles for colorimetric and fluorescent sensing of metal ions and biomolecules, *Coord. Chem. Rev.*, 2022, **459**, 214461.

10 P. Patil, K. V. Ajeya, M. P. Bhat, G. Sriram, J. Yu, H.-Y. Jung, T. Altalhi, M. Kigga and M. D. Kurkuri, Real-Time Probe for the Efficient Sensing of Inorganic Fluoride and Copper Ions

in Aqueous Media, *ChemistrySelect*, 2018, **3**(41), 11593–11600.

11 H.-H. Han, H. Tian, Y. Zang, A. C. Sedgwick, J. Li, J. L. Sessler, X.-P. He and T. D. James, Small-molecule fluorescence-based probes for interrogating major organ diseases, *Chem. Soc. Rev.*, 2021, **50**(17), 9391–9429.

12 X. Wang, Z. Wang, J. Cui, Y. Yao, M. Zheng, M. Zhang, L. Cao, Z. Yang, H. Suo and P. Li, Multifunctional Near-Infrared (NIR) Phosphors with NIR I and NIR II Luminescence for Biological Detection, *ACS Appl. Electron. Mater.*, 2022, **4**(1), 432–442.

13 Y. Wang, Z. Li, Q. Lin, Y. Wei, J. Wang, Y. Li, R. Yang and Q. Yuan, Highly Sensitive Detection of Bladder Cancer-Related miRNA in Urine Using Time-Gated Luminescent Biochip, *ACS Sens.*, 2019, **4**(8), 2124–2130.

14 J. Yin, L. Huang, L. Wu, J. Li, T. D. James and W. Lin, Small molecule based fluorescent chemosensors for imaging the microenvironment within specific cellular regions, *Chem. Soc. Rev.*, 2021, **50**(21), 12098–12150.

15 G.-Q. Jin, C. V. Chau, J. F. Arambula, S. Gao, J. L. Sessler and J.-L. Zhang, Lanthanide porphyrinoids as molecular theranostics, *Chem. Soc. Rev.*, 2022, **51**(14), 6177–6209.

16 J. Ning, H. Liu, X. Sun, G. Song, M. Shen, J. Liao, F. Su and Y. Tian, Rational Design of a Polymer-Based Ratiometric K^+ Indicator for High-Throughput Monitoring Intracellular K^+ Fluctuations, *ACS Appl. Bio Mater.*, 2021, **4**(2), 1731–1739.

17 M. Zhang, L. Gong, C. Sun, W. Li, Z. Chang and D. Qi, A new fluorescent-colorimetric chemosensor based on a Schiff base for detecting Cr^{3+}, Cu^{2+}, Fe^{3+} and Al^{3+} ions, *Spectrochim. Acta, Part A*, 2019, **214**, 7–13.

18 P. Thamaraiselvi, N. Duraipandy, M. S. Kiran and S. Easwaramoorthi, Triarylamine Rhodanine Derivatives as Red Emissive Sensor for Discriminative Detection of Ag^+ and Hg^{2+} ions in Buffer-Free Aqueous Solutions, *ACS Sustainable Chem. Eng.*, 2019, **7**(11), 9865–9874.

19 R. J. Lake, Z. Yang, J. Zhang and Y. Lu, DNAzymes as Activity-Based Sensors for Metal Ions: Recent Applications, Demonstrated Advantages, Current Challenges, and Future Directions, *Acc. Chem. Res.*, 2019, **52**(12), 3275–3286.

20 K. P. Carter, A. M. Young and A. E. Palmer, Fluorescent Sensors for Measuring Metal Ions in Living Systems, *Chem. Rev.*, 2014, **114**(8), 4564–4601.

21 J.-P. Dong, B. Li, Y.-J. Jin and L.-Y. Wang, Efficient detection of Fe(iii) and chromate ions in water using two robust lanthanide metal–organic frameworks, *CrystEngComm*, 2021, **23**(7), 1677–1683.

22 B. Wang, Q. Yang, C. Guo, Y. Sun, L.-H. Xie and J.-R. Li, Stable Zr(IV)-Based Metal–Organic Frameworks with Predesigned Functionalized Ligands for Highly Selective Detection of Fe(III) Ions in Water, *ACS Appl. Mater. Interfaces*, 2017, **9**(11), 10286–10295.

23 X.-H. Zhou, L. Li, H.-H. Li, A. Li, T. Yang and W. Huang, A flexible Eu(iii)-based metal–organic framework: turn-off luminescent sensor for the detection of Fe(iii) and picric acid, *Dalton Trans.*, 2013, **42**(34), 12403–12409.

24 N. Lehnert, E. Kim, H. T. Dong, J. B. Harland, A. P. Hunt, E. C. Manickas, K. M. Oakley, J. Pham, G. C. Reed and V. S. Alfaro, The Biologically Relevant Coordination Chemistry of Iron and Nitric Oxide: Electronic Structure and Reactivity, *Chem. Rev.*, 2021, **121**(24), 14682–14905.

25 E. C. Theil, T. Tosha and R. K. Behera, Solving Biology's Iron Chemistry Problem with Ferritin Protein Nanocages, *Acc. Chem. Res.*, 2016, **49**(5), 784–791.

26 X. Liu and E. C. Theil, Ferritins: Dynamic Management of Biological Iron and Oxygen Chemistry, *Acc. Chem. Res.*, 2005, **38**(3), 167–175.

27 J. Wang, T. Wang, Y. Hu, X. Zhang, Y. Ma, H. Lv, S. Xu, Y. Wang and Z. Jiang, Fe^{3+} sensitivity fluorescence sensor from β-cyclodextrin-enhanced Eu^{3+} luminescence aggregates, *J. Mater. Sci.*, 2021, **56**(18), 10979–10989.

28 M. Shellaiah, N. Thirumalaivasan, B. Aazaad, K. Awasthi, K. W. Sun, S.-P. Wu, M.-C. Lin and N. Ohta, Novel rhodamine probe for colorimetric and fluorescent detection of Fe3+ ions in aqueous media with cellular imaging, *Spectrochim. Acta, Part A*, 2020, **242**, 118757.

29 Z. Zuo, X. Song, D. Guo, Z. Guo and Q. Niu, A dual responsive colorimetric/fluorescent turn-on sensor for highly selective, sensitive and fast detection of Fe^{3+} ions and its applications, *J. Photochem. Photobiol., A*, 2019, **382**, 111876.

30 S. Zhou, M. Zhang, F. Yang, F. Wang and C. Wang, Facile synthesis of water soluble fluorescent metal (Pt, Au, Ag and Cu) quantum clusters for the selective detection of Fe^{3+} ions as both fluorescent and colorimetric probes, *J. Mater. Chem. C*, 2017, **5**(9), 2466–2473.

31 Y. Liu, W. Duan, W. Song, J. Liu, C. Ren, J. Wu, D. Liu and H. Chen, Red Emission B, N, S-co-Doped Carbon Dots for Colorimetric and Fluorescent Dual Mode Detection of Fe^{3+} Ions in Complex Biological Fluids and Living Cells, *ACS Appl. Mater. Interfaces*, 2017, **9**(14), 12663–12672.

32 M. K. Goshisht, G. K. Patra and N. Tripathi, Fluorescent Schiff base sensors as a versatile tool for metal ion detection: strategies, mechanistic insights, and applications, *Mater. Adv.*, 2022, **3**(6), 2612–2669.

33 M. Hasegawa, S. Sakurai, M. A. Yamaguchi, D. Iwasawa, N. Yajima, S. Ogata, Y. Inazuka, A. Ishii and K. Suzuki, Aspects of lanthanide complexes for selectivity, intensity and sharpness in luminescence bands from twenty-four praseodymium, europium and gadolinium complexes with differently distorted-hexadentate ligands, *Photochem. Photobiol. Sci.*, 2020, **19**(8), 1054–1062.

34 J. Feng and H. Zhang, Hybrid materials based on lanthanide organic complexes: a review, *Chem. Soc. Rev.*, 2013, **42**(1), 387–410.

35 W.-L. Chan, C. Xie, W.-S. Lo, J.-C. G. Bünzli, W.-K. Wong and K.-L. Wong, Lanthanide–tetrapyrrole complexes: synthesis, redox chemistry, photophysical properties, and photonic applications, *Chem. Soc. Rev.*, 2021, **50**(21), 12189–12257.

36 J. Duan, B. Ma, F. Liu, S. Zhang, S. Wang, Y. Kong, M. Du, L. Han, J. Wang, Y. Sang and H. Liu, Coordination ability determined transition metal ions substitution of Tb in Tb-Asp fluorescent nanocrystals and a facile ions-detection approach, *Nanoscale*, 2018, **10**(16), 7526–7535.

37 T. P. Gompa, A. Ramanathan, N. T. Rice and H. S. La Pierre, The chemical and physical properties of tetravalent

lanthanides: Pr, Nd, Tb, and Dy, *Dalton Trans.*, 2020, **49**(45), 15945–15987.

38 J. Wang, J. Liu, J. Wang, Y. Wang, J. Cao, L. Hou, R. Ge, J. Chi, L. Huang, J. Guo, A. R. Aleem, Z. Song, S. K. Tamang, J. Liu, G. Wang, M. J. Kipper, L. A. Belfiore and J. Tang, Smart sensing of Cu^{2+} in living cells by water-soluble and nontoxic Tb^{3+}/Eu^{3+}-induced aggregates of polysaccharides through fluorescence imaging, *J. Mater. Chem. C*, 2020, **8**(24), 8171–8182.

39 J. Hui, X. Zhang, Z. Zhang, S. Wang, L. Tao, Y. Wei and X. Wang, Fluoridated $HAp:Ln^{3+}$ (Ln = Eu or Tb) nanoparticles for cell-imaging, *Nanoscale*, 2012, **4**(22), 6967–6970.

40 T. Gunnlaugsson and J. P. Leonard, Responsive lanthanide luminescent cyclen complexes: from switching/sensing to supramolecular architectures, *Chem. Commun.*, 2005, (25), 3114–3131.

41 R. Goswami, T. K. Pal and S. Neogi, Stimuli -triggered fluoro-switching in metal–organic frameworks: applications and outlook, *Dalton Trans.*, 2021, **50**(12), 4067–4090.

42 A. R. Aleem, J. Liu, J. Wang, J. Wang, Y. Zhao, Y. Wang, Y. Wang, W. Wang, F. U. L. Rehman, M. J. Kipper and J. Tang, Selective Sensing of Cu^{2+} and Fe^{3+} Ions with Vis-Excitation using Fluorescent Eu^{3+}-Induced Aggregates of Polysaccharides (EIAP) in Mammalian Cells and Aqueous Systems, *J. Hazard. Mater.*, 2020, **399**, 122991.

43 L. Zhao, Z. Ren, X. Liu, Q. Ling, Z. Li and H. Gu, A Multifunctional, Self-Healing, Self-Adhesive, and Conductive Sodium Alginate/Poly(vinyl alcohol) Composite Hydrogel as a Flexible Strain Sensor, *ACS Appl. Mater. Interfaces*, 2021, **13**(9), 11344–11355.

44 Q. Li, M. Li, P. Zhu and S. Wei, In vitro synthesis of bioactive hydroxyapatite using sodium hyaluronate as a template, *J. Mater. Chem.*, 2012, **22**(38), 20257–20265.

45 J. A. Burdick and G. D. Prestwich, Hyaluronic acid hydrogels for biomedical applications, *Adv. Mater.*, 2011, **23**(12), 41–56.

46 Z. Song, J. Wang, J. Wang, J. Liu, X. Wang, Y. Wang, A. R. Aleem, M. J. Kipper, L. A. Belfiore and J. Tang, Eu^{3+}-induced polysaccharide nano-dumbbell aggregates (PNDA) as drug carriers to smartly report drug concentration through variable fluorescence, *Sens. Actuators, B*, 2021, **336**, 129724.

47 G. Ju, Y. Hu, L. Chen, X. Wang and Z. Mu, Concentration quenching of persistent luminescence, *Phys. B*, 2013, **415**, 1–4.

48 R. Gilli, M. Kacuráková, M. Mathlouthi, L. Navarini and S. Paoletti, FTIR studies of sodium hyaluronate and its oligomers in the amorphous solid phase and in aqueous solution, *Carbohydr. Res.*, 1994, **263**(2), 315–326.

49 A. G. Shard, M. C. Davies, S. J. B. Tendler, L. Bennedetti, M. D. Purbrick, A. J. Paul and G. Beamson, X-ray Photoelectron Spectroscopy and Time-of-Flight SIMS Investigations of Hyaluronic Acid Derivatives, *Langmuir*, 1997, **13**(10), 2808–2814.

50 P. P. Ferreira da Rosa, S. Miyazaki, H. Sakamoto, Y. Kitagawa, K. Miyata, T. Akama, M. Kobayashi, K. Fushimi, K. Onda, T. Taketsugu and Y. Hasegawa, Coordination Geometrical Effect on Ligand-to-Metal Charge Transfer-Dependent Energy Transfer Processes of Luminescent Eu(III) Complexes, *J. Phys. Chem. A*, 2021, **125**(1), 209–217.